PHYSICAL REVIEW B VOLUME 49, NUMBER 18 1 MAY 1994-II

Angular forces and melting in bcc transition metals: A case study of molybdenum

John A. Moriarty
Lawrence Livermore National Laboratory, University of California, Livermore, California 94551
(Received 20 September 1993)

Using multi-ion interatomic potentials derived from first-principles generalized pseudopotential theory (GPT) together with molecular-dynamics (MD) simulation, a detailed study of melting and related high-temperature solid and liquid properties in molybdenum has been performed. The energetics in such bcc transition metals are dominated by d-state interactions that give rise to both many-body angular forces and enhanced electron-thermal contributions. The angular forces are accounted for in the GPT through explicit three- and four-ion potentials, v_3 and v_4, which in the present work are applied in analytic model-GPT (MGPT) form. With the MGPT potentials, ion-thermal melting in Mo has been investigated both mechanically, by cycling up and down through the observed MD melting point at constant volume, and thermodynamically, by calculating solid and liquid free energies. In the former approach, parallel MD simulations have also been done with a corresponding effective-pair potential $v_2^{\rm eff}$ in which the angular dependence of v_3 and v_4 has been averaged. The multi-ion angular forces, which are essential to an accurate description of the bcc solid, are found to lower the dynamically observed melting point by about 1000 K. Above the melting transition, however, $v_2^{\rm eff}$ gives a reasonbly good account of the structure and thermal energy of the liquid and the accuracy of this description improves with increasing temperature. Both the multi-ion and effective pair potentials also permit a large amount of supercooling of the liquid before the onset of freezing. With $v_2^{\rm eff}$ a bcc structure is nucleated at freezing, while with the multi-ion potentials an amorphous glasslike structure is obtained, which appears to be related to the energetically competitive $A15$ structure. In our second approach to melting, the multi-ion potentials have been used to obtain accurate solid and liquid free energies from quasiharmonic lattice dynamics and MD calculations of thermal energies and pressures. The resulting ion-thermal melting curve exactly overlaps the dynamically observed melting point, indicating that no superheating of the solid occurred in our MD simulations. To obtain a full melting curve, electron-thermal contributions to the solid and liquid free energies are added in terms of the density of electronic states at the Fermi level, $\rho(E_F)$. Here the density of states for the solid has been calculated with the linear-muffin-tin-orbital method, while for the liquid tight-binding calculations have been used to justify a simple model. In the liquid $\rho(E_F)$ is increased dramatically over the bcc solid, and the net effect of the electron-thermal contributions is to lower the calculated melting temperatures by about a factor of 2. A full melting curve to 2 Mbar has thereby been obtained and the calculated melting properties near zero pressure are in generally good agreement with experiment.

I. INTRODUCTION

This paper concerns the high-temperature structural, thermodynamic, and melting properties of the bcc transition-metal molybdenum (Mo). There are three motivating factors behind this work. First, the high-pressure phase diagram of Mo is a problem of current experimental[1–4] and theoretical[1,5] interest. In this regard, there is now evidence that the bcc structure is destabilized at high pressure through one or more solid-solid phase transitions. Experimentally, a transition to an unknown structure has been observed at 2.1 Mbar and 4000 K from dynamic acoustic-velocity measurements.[1] Theoretically, a transition to an hcp structure has been predicted at 4.2 Mbar and 0 K from first-principles total-energy calculations.[5] In this paper, we focus on the high-temperature portion of the Mo phase diagram and the melting transition out of the bcc phase below about 2 Mbar.

A second motivating factor here is the related issue of metastability and the possible occurrence of one or more metastable solid phases at low pressure which are also relevant at high pressure. In the group-VB and -VIB bcc transition metals there is in fact one well-known metastable phase, namely, the low-symmetry $A15$ structure. This structure occurs quite frequently in the binary-alloy phase diagrams of these elements, e.g., in $\mathrm{Mo_3Si}$ and in Mo-Re and Mo-Os alloys. This phase has also been obtained in elemental tungsten (W) by the hydrogen reduction of $\mathrm{WO_3}$ and is alternately known as the β-W structure.[6] In addition, there is very recent experimental evidence in tantalum (Ta) that the $A15$ phase can be solidified from the supercooled liquid.[7] Theoretically, first-principles total-energy calculations[7–9] have verified the competitive nature of the $A15$ structure with bcc in Ta,[7] W,[7,8] and Mo.[8,9]

The third motivating factor in this work is the challenge of doing a realistic microscopic melting calculation on a complex d-band material. In this regard, the melting properties of central transition metals are complicated by two important factors not present in simple systems. First, there is the presence of angular forces arising from d-state interactions and abundantly evident in the solid structural and vibrational properties of these materials. We take such forces into account here through explicit three- and four-ion interatomic potentials, v_3 and v_4. These potentials arise from a first-principles, multi-ion expansion of the cohesive-energy functional for the bulk metal of the order-N-scaling form

$$E_{\rm coh}(\mathbf{R}_1\cdots\mathbf{R}_N)=E_{\rm vol}(\Omega)+\frac{1}{2N}\sum_{i,j}{}'v_2(ij)+\frac{1}{6N}\sum_{i,j,k}{}'v_3(ijk)+\frac{1}{24N}\sum_{i,j,k,l}{}'v_4(ijkl)\ , \tag{1}$$

where Ω is the atomic volume, the sums are over all N ion positions, and the prime on each summation excludes those contributions where two site indices are equal. This expansion has been derived for transition metals via generalized pseudopotential theory (GPT),[10] starting from fundamental quantum mechanics in the local-density approximation (LDA).[11] The leading volume term $E_{\rm vol}$ includes all one-ion *intra-atomic* contributions to the cohesive energy, while the interatomic potentials v_2, v_3, and v_4 are expressible in terms of weak pseudopotential and d-state tight-binding and hybridization matrix elements coupling different sites. These interatomic potentials are volume dependent but *structure independent* and thus rigorously transferable at a given volume to all bulk structures, including the liquid. In this work, we utilize the expansion (1) in the simplified model—GPT (MGPT) form,[12] where v_3 and v_4 have been reduced to entirely analytic expressions. This allows us to do direct molecular-dynamics (MD) simulation of both the high-temperature solid and the liquid, which heretofore has not been possible. To expose the role of the angular forces explicitly, we have also done parallel calculations with an effective-pair potential $v_2^{\rm eff}$, in which v_3 and v_4 are averaged and combined with v_2.

The other complicating factor in transition-metal melting is the presence of a very large electron-thermal component to the liquid free energy. This arises from the large d-state electronic density of states (DOS) at the Fermi level E_F, as evidenced by the high measured specific heats $c_p^{\rm liq}$ in liquid transition metals. In simple metals, one typically observes $c_p^{\rm liq}$ in the range of 3–4 k_B, whereas in group-VB and -VIB metals $c_p^{\rm liq}$ is measured in the range of 4–9 k_B.[13–18] In the group-VIB metals such as Mo, the impact of the density of states on melting is particularly large because, in contrast to the liquid, E_F for the solid sits in the middle of a deep valley of the corresponding bcc DOS. Thus there is a big *increase* in the DOS upon melting and a big *decrease* in the free energy. As we shall demonstrate in this paper, this effect lowers the calculated melting temperatures of Mo by about a factor of 2. Nonetheless, one still has the usual condition $k_BT \ll E_F$ near melting, so that ion- and electron-thermal contributions to the free energy may be considered separately. In this work, we incorporate electron-thermal contributions through appropriate calculations of the solid and liquid DOS for Mo. In the bcc solid we perform direct self-consistent linear-muffin-tin-orbital[19,20] (LMTO) calculations. In the liquid, on the other hand, we use canonical-d-band, tight-binding calculations to justify a simple, but realistic model DOS.

The outline of this paper is as follows. In Sec. II we first discuss the refined and specialized MGPT interatomic potentials which have been developed for Mo in connection with the present study. Next in Sec. III we present the results of our rather extensive MD studies of the high-temperature solid and liquid using these potentials, including dynamically observed melting and freezing and the calculation of free energies and the ion-thermal melting curve in the absence of electron-thermal contributions. In Sec. IV we then consider the electronic DOS for bcc and liquid Mo and the calculation of the full melting curve and associated melting properties. We conclude in Sec. V.

II. MGPT INTERATOMIC POTENTIALS

The derivation of the simplified MGPT version of Eq. (1) from the first-principles theory is discussed at length in Ref. 12. In this section we briefly review some of the salient features of this approach and discuss the specific interatomic potentials we have developed for the present study on Mo. The formal character of the potentials v_2, v_3, and v_4 is the same in the MGPT as in the full GPT. At constant volume Ω, the central-force pair potential v_2 is a one-dimensional function of the ion-ion separation distance $R_{ij}=|\mathbf{R}_i-\mathbf{R}_j|$:

$$v_2(ij)\equiv v_2(R_{ij};\Omega)\ , \tag{2}$$

while the angular-force triplet potential v_3 and quadruplet potential v_4 are, respectively, the three- and six-dimensional functions

$$v_3(ijk)\equiv v_3(R_{ij},R_{jk},R_{ki};\Omega) \tag{3}$$

and

$$v_4(ijkl)\equiv v_4(R_{ij},R_{jk},R_{kl},R_{li},R_{ki},R_{lj};\Omega)\ . \tag{4}$$

In the full GPT, however, v_2, v_3, and v_4 are all nonanalytic functions, so that the multidimensional potentials v_3 and v_4 cannot be readily tabulated for application purposes. This is the major problem overcome in the MGPT, where v_3 and v_4 are approximated by analytic forms, based on canonical d bands, that retain the dominant physics of the full theory.

As discussed in Ref. 12, the approximations used in the MGPT are explicitly tailored for central transition metals such as Mo, where the emphasis is on direct, short-range d-d interactions between ions and indirect, long-range sp-d hybridization interactions between ions play a secondary role. In particular, the MGPT contributions to v_3 and v_4 arise entirely for such short-range d-state interactions, and it is appropriate to treat the corresponding contribution to v_2 on the same footing. The total two-ion pair potential is thereby reduced to the form

$$v_2(r)=v_2^{\rm sp}(r)+v_2^{\rm hc}(r)+v_2^d(r)\ , \tag{5}$$

where $v_2(r)\equiv v_2(r;\Omega)$, etc. at constant volume Ω. Here both the simple-metal component $v_2^{\rm sp}$, which derives from s- and p-electron interactions, and the hard-core component $v_2^{\rm hc}$, which derives from d-state nonorthogonality, are retained directly from the first-principles theory. An analytic form for the remaining d-state component v_2^d is developed by first approximating the direct tight-binding-like matrix elements between d states as

$$\Delta_{dd'}^{\rm vol}(R_{ij})=\alpha_m(R_{\rm WS}/R_{ij})^p\ , \tag{6}$$

where the coefficients α_m have the 6:−4:1 ratio of canonical d bands for $m=0$, 1, and 2; $R_{\rm WS}$ is the Wigner-Seitz radius; and p is a material-dependent constant. For pure canonical d bands, $p=2l+1=5$ with $l=2$, but the choice $p=4$ is closer to the first principles GPT for the Mo and is retained as a desirable improvement. Using Eq. (6), one derives

$$\begin{aligned}v_2^d(r)&=v_a[f(r)]^4-v_b[f(r)]^2\\&=v_a(r_0/r)^{4p}-v_b(r_0/r)^{2p}\ ,\end{aligned} \tag{7}$$

where

$$f(r)\equiv(r_0/r)^p \tag{8}$$

is a characteristic radial function, with $r_0\equiv1.8R_{\rm WS}$. The quantities v_a and v_b are material parameters which depend primarily on d-band filling and width. From general theoretical considerations, one expects that for the central transition metals $v_a>0$ and $v_b>0$ with $v_b\gg v_a$, so that v_2^d is an entirely attractive potential in the physical region of interest. In addition, v_2^d dominates $v_2^{\rm sp}$ and $v_2^{\rm hc}$ over this regime, so that v_2 is also attractive at all near-neighbor distances.

Analytic expressions for v_3 and v_4 are also derived starting from Eq. (6). For v_3 one obtains the result

$$\begin{aligned}v_3(r_1,r_2,r_3)=v_cf(r_1)f(r_2)f(r_3)L(\theta_1,\theta_2,\theta_3)\\+v_d\{[f(r_1)f(r_2)]^2P(\theta_3)\\+[f(r_2)f(r_3)]^2P(\theta_1)\\+[f(r_3)f(r_1)]^2P(\theta_2)\}\ ,\end{aligned} \tag{9}$$

where θ_1, θ_2, and θ_3 are the angles subtended by r_1, r_2, and r_3, as shown in Fig. 4 of Ref. 12. Both L and P are universal angular functions which depend only on d symmetry and apply to all transition metals. Their analytic forms are given by Eqs. (50) and (51), respectively, of Ref. 12. The coefficients v_c and v_d in Eq. (9) are additional material parameters that again mostly reflect d-band filling and width. For almost half-filled d bands, v_c is near zero while v_d is positive, so that $v_d\gg|v_c|$ and v_3 is an entirely repulsive potential, which tends to balance the attractive v_2 in the region of near-neighbor interactions.

For v_4, on the other hand, one obtains the oscillatory potential

$$\begin{aligned}v_4(r_1,r_2,r_3,r_4,r_5,r_6)=v_e[&f(r_1)f(r_2)f(r_4)f(r_5)M(\theta_1,\theta_2,\theta_3,\theta_4,\theta_5,\theta_6)\\&+f(r_3)f(r_2)f(r_6)f(r_5)M(\theta_7,\theta_8,\theta_9,\theta_{10},\theta_5,\theta_{12})\\&+f(r_1)f(r_6)f(r_4)f(r_3)M(\theta_{11},\theta_{12},\theta_5,\theta_6,\theta_3,\theta_4)]\ ,\end{aligned} \tag{10}$$

where M is a third universal angular function which depends only upon d symmetry and v_e is an additional material parameter. The full analytic result for M is given in Appendix B of Ref. 12, while the precise definitions of the six distances $r_1\cdots r_6$ and 12 angles $\theta_1\cdots\theta_{12}$ associated with four-ion geometry are given in Fig. 6 of that paper. The angular dependence of v_4 is highly commensurate with the bcc structure, and for nearly half-filled d bands with $v_e>0$, this potential makes a large contribution to bcc stability.

In this work, we also wish to consider to what extent the MGPT three- and four-ion potentials, Eqs. (9) and (10), can be folded down into an effective pair potential to eliminate any explicit angular dependence in the cohesive-energy functional. Such an effective-pair potential can be obtained by averaging over the multi-ion potentials:

$$v_2^{\rm eff}=v_2+\langle v_3\rangle+\langle v_4\rangle\ . \tag{11}$$

The oscillatory nature of v_4 makes its net contribution to $v_2^{\rm eff}$ negligibly small. For the case of a nearly half-filled d-band metals such as Mo, one can also neglect the three-ion contribution involving v_c. The remaining contributions from $\langle v_3\rangle$ produce terms proportional to $f^2(r)$, as already appear in v_2, so that one obtains a form

$$\begin{aligned}v_2^{\rm eff}(r)=v_2^{\rm sp}(r)+v_2^{\rm hc}(r)+v_a^*(r_0/r)^{4p}\\-v_b^*(r_0/r)^{2p}\ ,\end{aligned} \tag{12}$$

where $v_a^*\simeq v_a$, but $v_b^*\ll v_b$ since the repulsive nature of v_3 has now been folded back into v_b^*.

In actually applying the interatomic potentials of the MGPT to the calculation of physical properties, we include a smooth Gaussian cutoff of the functions $f(r)$ and $v_2^{\rm sp}(r)$ at large r. For $f(r)$ we take

$$f(r)=\begin{cases}(r_0/r)^p & r<R_0\\(r_0/r)^p\exp[-\alpha(r/R_0-1)^2] & r>R_0\ ,\end{cases} \tag{13}$$

where $R_0=2.15R_{\rm WS}$ and $\alpha\gg1$. This ensures that direct interactions between ions are highly damped beyond the second-nearest-neighbor distance in the bcc structure. We also assume that v_2 is damped at long range in the same manner as v_2^d, so that for $r > R_0$, $v_2(r)$ is replaced by $v_2(r)\exp[-2\alpha(r/R_0-1)^2]$. The latter replacement has negligible effect on v_2^{hc} but has the physically correct effect of suppressing the weak Friedel oscillations contained in v_2^{sp}. The same damping scheme is also applied to v_2^{eff}.

The material parameters v_a, v_b, v_c, v_d, and v_e appearing in the MGPT multi-ion potentials can be determined in a variety of ways using a combination of rigorous theoretical constraints, first-principles GPT and LMTO calculational results, and experimental data. All schemes examined in Ref. 12 for Mo yield potentials which are qualitatively similar to each other as well as those of the first-principles GPT. In this work we follow scheme 1 of Ref. 12, but with several important modifications and refinements.

(i) The magnitude of the dimensionless damping parameter α in Eq. (13) has been increased from 25 to 125. This renders direct third-neighbor bcc and second-neighbor fcc or hcp interactions completely negligible and reduces the number of neighbors a given ion interacts with via v_3 and v_4 to 64 for the bcc structure. This reduced range is essential for tractable MD simulations, but it comes at the expense of worsening some calculated properties which are sensitive to long-range d-state interactions such as the hcp-fcc energy difference and the zone-boundary [100] phonons.

(ii) The first-principles volume term $E_{\text{vol}}(\Omega)$ used in Ref. 12 has been modified to be more consistent with the actual fitted potential coefficients v_α ($\alpha = a$, b, c, d, or e). Specifically, $E_{\text{vol}}(\Omega)$ is now constrained so that, for a given cohesion curve $E_{\text{coh}}(\Omega)$, each coefficient v_α will maintain an approximate linear variation with d-band width, $W_d \propto (\Omega)^{-p/3}$, under either compression or expansion. This behavior is expected on theoretical grounds, and the resulting calculated volume dependence of structural energies, elastic constants, and phonons is thereby significantly improved.

(iii) The numerical accuracy of the second-derivative, multi-ion radial force-constant functions $K_r^{(n)}$ [Eq. (78) of Ref. 12] used to calculate elastic constants and phonons has been improved for $n \geq 3$. The major impact of this refinement is that one generally requires a larger value of v_e/v_d to reproduce a given elastic constant or phonon frequency. The larger v_e/v_d in turn increases the calculated bcc-fcc energy difference and brings it into better agreement with first-principles results.

A summary of calculated properties for bcc Mo obtained with the present modified scheme 1 is given in Table I and compared with both experiment[21–27] and LDA band-theory results.[12,28–30] In addition to the improved bcc-fcc energy difference, there is also noteworthy improvement in the pressure derivatives of the elastic constants. On the other hand, our overestimate of the longitudinal zone-boundary [100] phonon frequency leads to an 8% overestimate of the Debye temperature and a corresponding underestimate of the Grüneisen parameter. In the present context, this ultimately means that we will overestimate the melting temperature of the bcc solid somewhat, but otherwise these quantitative shortcomings

TABLE I. Physical properties of bulk bcc Mo. Quantities and units: cohesive energy E_{coh} and vacancy-formation energy E_{vac} in Ry; equilibrium atomic volume Ω_{eq} and vacancy volume Ω_{vac} in a.u.; bulk modulus B and elastic constants (C_{11}, C_{44}, C_{12}, and C') in Mbar; structural energies is mRy; longitudinal (L) and transverse (T_1 and T_2) phonon frequencies in THz; Debye temperature Θ_D in K; and dimensionless Grüneisen parameter γ_G. Phonon frequencies are Brillouin-zone-boundary values except as indicated. All of the present theoretical quantities except Ω_{eq} are evaluated at the observed equilibrium atomic volume $\Omega_0 = 105.1$ a.u.

	v_2^{eff}	v_2, v_3, v_4	Experiment	Band theory
		Cohesion		
E_{coh}	-0.614	-0.664	-0.501[c]	-0.455[d]
Ω_{eq}	105.2	105.2	105.1	105.2
B	2.64[a]	2.64[a]	2.64[e]	2.64
$\partial B/\partial P$	4.42	4.42	4.44[f]	4.42
		Vacancy formation		
E_{vac}	0.28	0.23[a]	0.23[g]	
$\Omega_{\text{vac}}/\Omega_0$	0.68	0.67		
		Structural phase stability		
bcc-fcc	-7.7	-30.4		-30.0[d]
hcp-fcc	0.0	0.05		2.0
		Elastic constants		
C_{11}	2.66	4.66[a]	4.66[e]	4.40[h]
C_{44}	2.38	1.10[a]	1.10	1.39
C_{12}	2.63	1.63	1.63	1.62
C'	0.02	1.51	1.52	1.39
$\partial C_{11}/\partial P$	4.46	6.22	6.41[f]	
$\partial C_{44}/\partial P$	2.46	1.22	1.40	
$\partial C_{12}/\partial P$	4.41	3.53	3.45	
$\partial C'/\partial P$	0.02	1.34	1.48	
		Phonon frequencies		
$L[\zeta 00]$[b]	7.93	9.34	7.61[i]	
$L[100]$	9.51	9.20	5.52	5.0[j]
$L[110]$	10.03	8.11	8.14	
$T_1[110]$	0.57	6.13	5.73	5.8[k]
$T_2[110]$	6.91	4.02	4.56	4.0[k]
$L[\xi\xi\xi]$[b]	4.63	6.32	6.16	6.1[j]
		Phonon averages		
Θ_D	395.0[a]	395.0	367.0[i]	
γ_G	1.46	1.44	1.55[f]	

[a] Fixed or fitted quantity.

[b] In $L[\zeta 00]$, $\zeta = \frac{3}{5}$; in $L[\xi\xi\xi]$, $\xi = \frac{2}{3}$.

[c] Reference 21.

[d] Parallel LMTO results, as described in Ref. 12.

[e] Room-temperature data of Ref. 22.

[f] Room-temperature data of Ref. 23.

[g] Average value from the data of Refs. 24–26.

[h] Reference 28.

[i] Room-temperature data of Ref. 27.

[j] Reference 29.

[k] Reference 30.

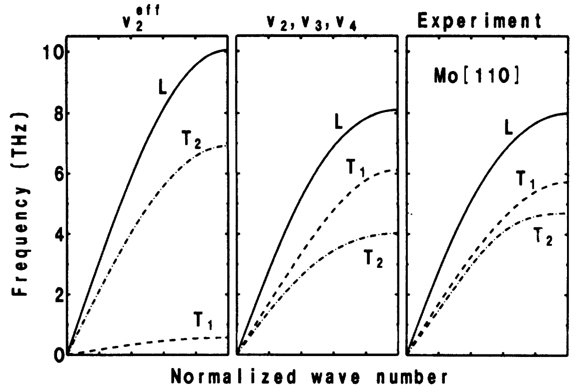

FIG. 1. Phonon frequencies in bcc Mo along the [110] direction. Left panel: as calculated from the effective-pair potential v_2^{eff}; central panel: as calculated from the multi-ion potentials v_2, v_3, and v_4; right panel: as measured experimentally from Ref. 27.

will not adversely affect our study.

To emphasize the importance of the angular forces contained in v_3 and v_4 to the solid structural properties of Mo, we have calculated the same quantities with the effective-pair potential v_2^{eff}. These results are also listed in Table I. Here we have used the same modified volume term as discussed above and have constrained the potential parameters v_a^* and v_b^* in Eq. (12) to yield the same cohesion curve and Debye temperature as with v_2, v_3, and v_4. While the effective-pair-potential model readily accommodates such average properties of the solid, it will inevitably yield a poor description of structural energies, elastic constants, and phonons, as shown in Table I. In this regard, the bcc-fcc energy difference is underestimated by a factor of 4 with v_2^{eff}, while the elastic constants and phonons display behavior that is more typical of a simple metal than a central transition metal. The latter is most apparent by examining the phonons in the [110] direction, as illustrated in Fig. 1. With v_2^{eff} one obtains a very soft transverse T_1 branch, lying far below the T_2 branch, and a correspondingly small C' shear elastic constant ($C_{44} \gg C'$), whereas with v_2, v_3, and v_4 one properly obtains a stiff T_1 branch, lying above the T_2 branch, and a large C' constant ($C' > C_{44}$).

III. MOLECULAR-DYNAMICS SIMULATION OF ION-THERMAL PROPERTIES

In calculating the thermodynamic properties of metals, it is convenient to separate zero-temperature, ion-thermal, and electron-thermal components. For example, the total internal energy and pressure as a function of volume Ω and temperature T can be written

$$E(\Omega,T)=E_0(\Omega)+E_{\text{ion}}(\Omega,T)+E_{\text{el}}(\Omega,T) \tag{14}$$

and

$$P(\Omega,T)=P_0(\Omega)+P_{\text{ion}}(\Omega,T)+P_{\text{el}}(\Omega,T) , \tag{15}$$

respectively. In the present context, the zero-temperature energy and pressure may be defined as the static contributions $E_0=E_{\text{coh}}^0$ and $P_0=-dE_{\text{coh}}^0/d\Omega$ obtained from Eq. (1) for the bcc structure. The ion thermal components E_{ion} and P_{ion} are then the excess energy and pressure derived from Eq. (1) at finite temperature T, and it is to these components we address ourselves in this section. The additional electron-thermal components E_{el} and P_{el}, arising from the thermal excitation of electrons above the Fermi level, will be considered in Sec. IV.

Our primary computational tool for investigating the high-temperature ion-thermal properties of Mo is molecular-dynamics simulation. In this regard, the major complication in using MGPT multi-ion potentials for MD calculations comes in the specification of the position-dependent force $\mathbf{F}_i$ on each ion i, and it is essential to exploit the inherent symmetries of the potentials v_2, v_3, and v_4 to obtain an efficient scheme. As is well known, the pair component of the force at constant volume, $\mathbf{F}_i^{(2)}$, can be expressed in term of the single radial derivative of v_2:

$$\mathbf{F}_i^{(2)}=-\sum_j{}' \frac{\partial v_2(ij)}{\partial \mathbf{R}_i}=-\sum_j{}' \frac{\partial v_2(ij)}{\partial R_{ij}}\frac{\partial R_{ij}}{\partial \mathbf{R}_i}$$
$$=-\sum_j{}' \frac{\partial v_2(ij)}{\partial R_{ij}}\hat{\mathbf{R}}_{ij} , \tag{16}$$

where $\hat{\mathbf{R}}_{ij}$ is the unit vector $(\mathbf{R}_i-\mathbf{R}_j)/R_{ij}$. What is perhaps less obvious, however, is that this result can be generalized to the multi-ion potentials v_3 and v_4. Using only the fact that $v_3(ijk)$ and $v_4(ijkl)$ are symmetric with respect to the interchange of any two indices, one can derive the corresponding results

$$\mathbf{F}_i^{(3)}=-\sum_{j,k}{}' \frac{\partial v_3(ijk)}{\partial R_{ij}}\hat{\mathbf{R}}_{ij} \tag{17}$$

and

$$\mathbf{F}_i^{(4)}=-\frac{1}{2}\sum_{j,k,l}{}' \frac{\partial v_4(ijkl)}{\partial R_{ij}}\hat{\mathbf{R}}_{ij} . \tag{18}$$

Thus even for v_3 and v_4 only a single radial derivative of the potential must be calculated to express a contribution to the force. Moreover, because v_3 and v_4 are analytic functions in the MGPT, these derivatives can be computed very accurately. The derivation of Eqs. (17) and (18) is discussed in the Appendix together with additional details on how one can exploit these results to obtain an efficient MD calculational scheme. Heretofore, the only computer simulation using MGPT potentials[31] has been performed with a Monte-Carlo method, which requires just the cohesive-energy functional (1).

Once the forces are specified, standard methods can be used to perform the MD simulations. In the present study, we have generally treated 250 ions in a constant-Ω, constant-T ensemble. Constant volume Ω is maintained by performing each simulation in a cubic box of length 10.1549 R_{WS} with periodic boundary conditions applied to the sides of the box. Constant temperature T is maintained with a Gaussian thermostat,[32–34] which is introduced through a friction term in modified Newtonian equations of motion for the ions:

$$\ddot{\mathbf{R}}_i=\mathbf{F}_i/m-\xi\dot{\mathbf{R}}_i \;, \tag{19}$$

where

$$\mathbf{F}_i=\mathbf{F}_i^{(2)}+\mathbf{F}_i^{(3)}+\mathbf{F}_i^{(4)} \tag{20}$$

is the total force on ion i and the effective friction coefficient ξ is given by

$$\xi=\sum_j \dot{\mathbf{R}}_j\cdot(\mathbf{F}_j/m)/\sum_j \dot{\mathbf{R}}_j\cdot\dot{\mathbf{R}}_j \;. \tag{21}$$

We have solved the coupled equations of motion (19) with a standard velocity-Verlet algorithm[33] using a time step of approximately 2×10^{-15} sec (2 femtoseconds). This scheme has been chosen here for its basic simplicity and its reliability in producing highly stable results over wide ranges of volume and temperature. The same scheme has also been applied in the effective-pair-potential case, where, of course, the total force is just $\mathbf{F}_i^{(2)}$ given by Eq. (16) with v_2 replaced by v_2^{eff}.

In a typical simulation, we begin with positions and scaled velocities for the ions from a previously equilibrated run at the same volume and a nearby temperature. We then run 4000–8000 time steps to establish a good thermodynamic equilibrium and an additional 8000 time steps to gather statistics for the calculation of various thermodynamic and structural properties. The most important thermodynamic quantities we obtain are the ion-thermal energy and pressure introduced above:

$$E_{\text{ion}}(\Omega,T)=\langle E_{\text{coh}}\rangle-E_{\text{coh}}^0 \tag{22}$$

and

$$P_{\text{ion}}(\Omega,T)=\langle -dE_{\text{coh}}/d\Omega\rangle+dE_{\text{coh}}^0/d\Omega \;, \tag{23}$$

where $\langle\cdots\rangle$ denotes a thermal average over the 250-ion ensemble. The most important structural quantities we obtain are the standard pair-correlation function $g(r)$ and an angular-correlation function $b(\theta)$. The latter is taken to be the number of bond angles a given ion makes with its near neighbors. Specifically, a bond angle θ for ion i with neighbors j and k is here defined as

$$\theta=\cos^{-1}[\mathbf{R}_{ij}\cdot\mathbf{R}_{ik}/(R_{ij}R_{ij})] \;, \tag{24}$$

where both R_{ij} and R_{ij} are required to be less than some given radius $R_{\max}$. We choose $R_{\max}=2.3\;R_{\text{WS}}$, so that both first- and second-neighbor bond angles are included for the bcc structure. The quantity $b(\theta)$ is an especially useful tool for investigating the local atomic structure about an ion.

A. Dynamic melting and cooling at constant volume

The investigation of melting in Mo has been approached in two closely related ways. In the first approach, we have cycled up and down through the dynamically observed melting point at a constant volume $\Omega=\Omega_0$, doing parallel calculations with the multi-ion potentials and with the effective-pair potential. Beginning at 500 K, the temperature has been raised in increments of 1500 K until the vicinity of melting, where the increment has been reduced to 250 K and much longer runs performed. Figure 2 illustrates the behavior of the angular-correlation function $b(\theta)$ at 500, 3500, and 6500 K in the bcc solid. At 500 K there are six well defined bond angles near 54.7, 70.5, 90, 109.5, 125.3, and 180 de-

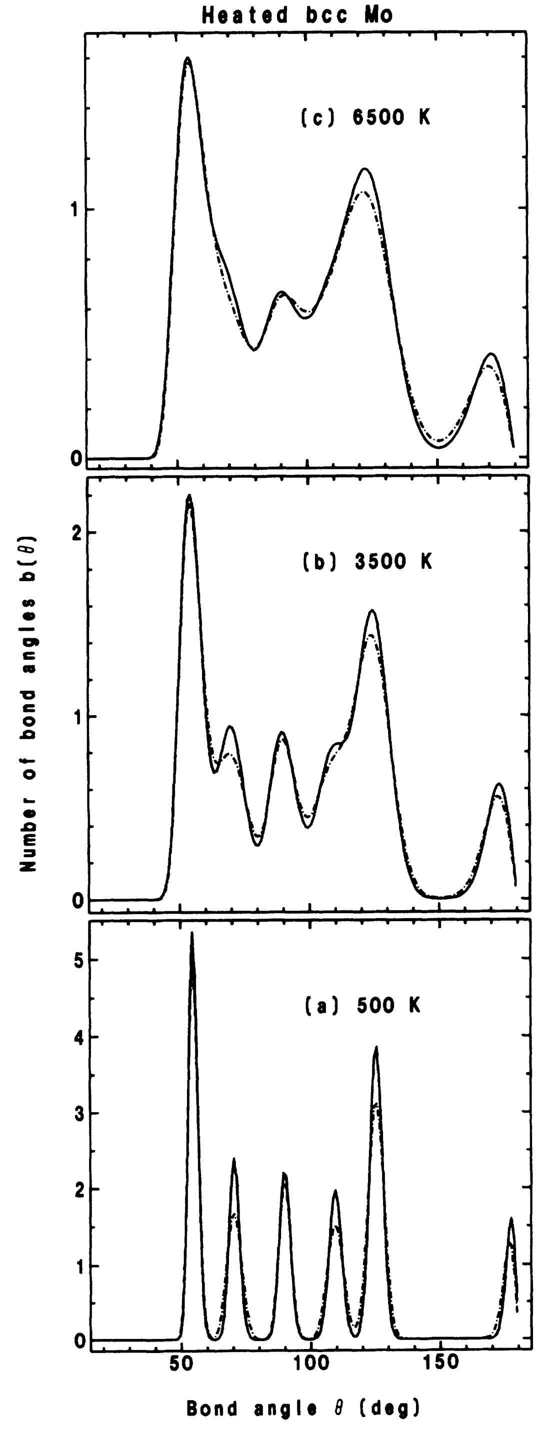

FIG. 2. Angular-correlation function $b(\theta)$ for bcc Mo heated to three temperatures at $\Omega=\Omega_0$, as obtained with the multi-ion potentials v_2, v_3, and v_4 (solid curves) and with the effective-pair potential v_2^{eff} (dot-dashed curves). (a) 500 K; (b) 3500 K; (c) 6500 K.

grees, as is characteristic of the static bcc structure. Note that the multi-ion and effective-pair potentials yield similar behavior, although the peaks in $b(\theta)$ are generally sharper with the former than with the latter. At higher temperature the peaks in both cases rapidly broaden and eventually begin to merge, such that at 6500 K only four clearly defined peaks remain. One clear signature of ion-thermal melting turns out to be loss of two of the remaining peaks at 90 and 180 degrees. This is found to occur at 8750 K for the multi-ion-potential case and at 9750 K for the effective-pair-potential case. In this regard, the dynamic ion-thermal melting transition is found to be rather sharp and well defined and is readily indicated in all quantities we monitor, so that is relatively little uncertainty in where it actually occurs. The corresponding average melting pressures are approximately 0.30 Mbar in the multi-ion-potential case and 0.28 Mbar in the effective-pair-potential case.

Once in the liquid, we have proceeded both upwards and downwards in temperature in increments of 3000 K. Figure 3 shows our calculated pair-correlation and angular-correlation functions for liquid Mo at 9500 K near the melting point. The pair-correlation functions $g(r)$ at this temperature and above displays qualitative behavior that is fairly typical of most liquid metals, with no major new features arising from the angular forces. Small qualitative differences are seen in the first two peaks of $g(r)$ obtained via v_2, v_3, and v_4 and via v_2^{eff}, respectively, but these differences lessen continuously with

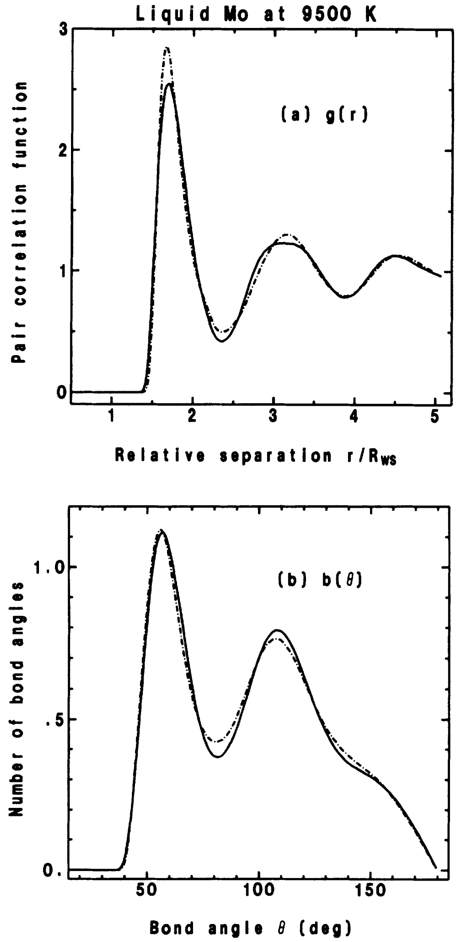

FIG. 3. (a) Pair-correlation function $g(r)$ and (b) angular-correlation function $b(\theta)$ for liquid Mo at 9500 K and $\Omega=\Omega_0$, as obtained with the multi-ion potentials v_2, v_3, and v_4 (solid curves) and with the effective-pair potential v_2^{eff} (dot-dashed curves).

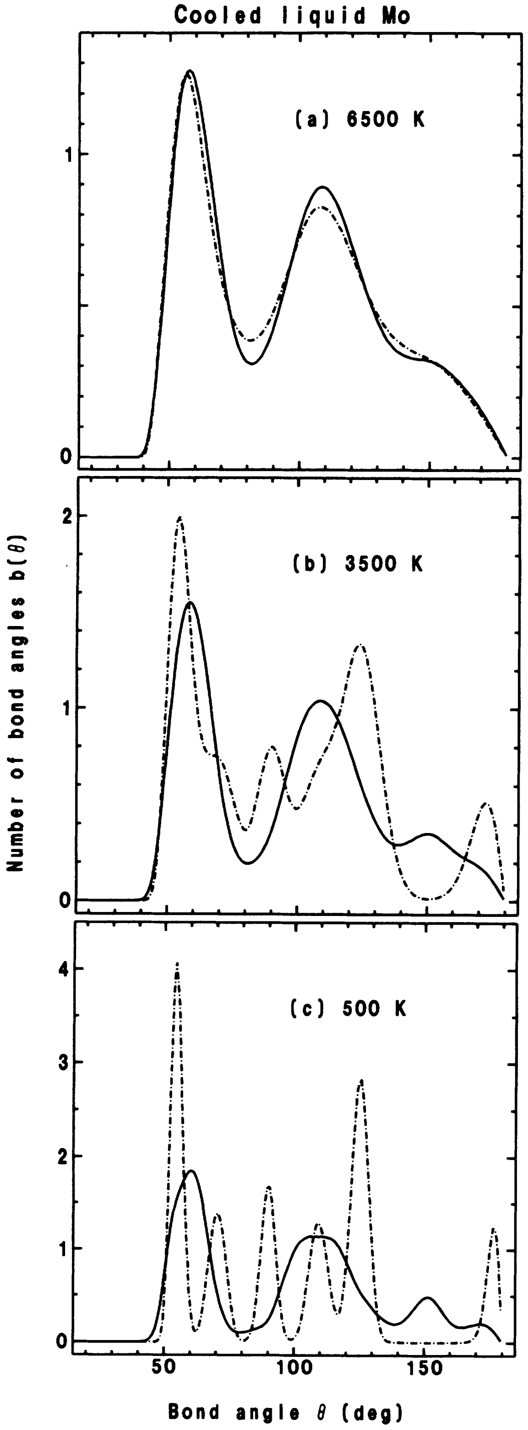

FIG. 4. Angular-correlation functions $b(\theta)$ for liquid Mo cooled to three temperatures from 9500 K in increments of 3000 K at $\Omega=\Omega_0$, with the solid and dot-dashed line as in Fig. 2. (a) 6500 K; (b) 3500 K; (c) 500 K.

increasing temperature. This convergence is also reflected in calculated thermodynamic properties, and in particular, above 15 500 K the two respective ion-thermal energies become almost indistinguishable. The latter fact can be used to considerable advantage in calculating liquid free energies, as will be discussed below. With regards to the angular-correlation function $b(\theta)$, a prominent two-peaked structure is retained in the liquid. Again only small differences are seen between the multi-ion-potential and effective-pair-potential $b(\theta)$, indicating that the local atomic structure of the liquid is well described by v_2^{eff}. The two peaks in $b(\theta)$ begin to coalesce into a single peak at higher temperature, but at 50 000 K, the upper temperature limit of our calculations,[35] separate peaks can still be distinguished.

Two of the most interesting findings in our MD simulations are the large degree to which liquid Mo can be undercooled or supercooled below the ion-thermal melting point and the very contrasting behavior obtained between the multi-ion and effective-pair potentials near freezing. Figure 4 shows our calculated results for $b(\theta)$ obtained from sequentially cooling the liquid from 9500 K to 6500, 3500, and 500 K. At 6500 K the metal is clearly still very liquid like in both cases, and the onset of freezing only occurs below about 4000 K. In the effective-pair-potential case, a bcc structure is nucleated from the liquid below this point, as is evident by comparing Fig. 4 with Fig. 2 at 3500 and 500 K. Interestingly, the shape and size of the computational cell appear to play no direct role in this outcome, as the nucleated bcc structure is oriented at an arbitrary angle with respect to the cubic axes of the cell. Also in this regard, close inspection of Fig. 4(c) clearly reveals that a perfect bcc structure is not recovered, although the detailed nature of its defects remains to be investigated. In the multi-ion-potential case, on the other hand, the liquid freezes into an amorphous glasslike structure which appears to contain at least one important feature in common with the *A* 15 lattice. Specifically, the peak in $b(\theta)$ which develops near 150 degrees, while totally absent for the bcc structure, is present in the form of a double peak for the pure *A* 15 structure, as illustrated in Fig. 5. This latter result was obtained from a 216-ion cubic-cell simulation at 500 K with the ion positions initialized on the *A* 15 lattice.

The contrasting freezing behavior of the multi-ion and effective-pair potentials is consistent with the static structural energetics exhibited by these potentials. In the effective-pair-potential case, there are no apparent solid phases which are both energetically competitive with bcc and mechanically stable. The *A* 15 structure in this case has a considerably higher energy than bcc over a wide volume range and is almost certainly mechanically unstable. In the multi-ion-potential case, on the other hand, the *A* 15 structure is found to be both mechanically stable, as indicated in Fig. 5, and almost degenerate in energy with bcc over the same volume range, with the *A* 15 phase actually slightly favored over bcc near Ω_0 and at larger volumes. Again this is a situation where the angular dependence of v_4 is highly favorable for the *A* 15 structure with $v_e > 0$. The actual ordering obtained between the bcc and *A* 15 phases is a rather sensitive artifact of the multi-ion-potential details and in the future it may be useful to impose the correct ordering as a constraint on the potentials. Regardless, the competitive nature of the *A* 15 and bcc structures exhibited by the present potentials is physically correct and has encouraged us to explore further the question of whether or not either of these structures could be nucleated from the liquid. To do this we have examined the effect of both the cooling schedule and the computational-cell size on our MD simulations of freezing. With regard to cooling schedule, we have performed two additional calculations with both a faster and a slower cooling rate. In the first a direct quench was done from 9500 to 500 K, while in the second the liquid was cooled between these temperatures at the rate of 1 K per time step or 5×10^{14} K/sec. In both calculations the same amorphous structure was obtained, suggesting little sensitivity of the result to cooling rate, at least for rates above 10^{14} K/sec. Using the slower cooling rate, we then proceeded to repeat the simulations for 216- and 432-ion computational cells. (The 216-ion cubic cell is commensurate with the *A* 15 structure, while the 250- and 432-ion cells are commensurate with bcc.) In both simulations, however, the same amorphous structure was again nucleated. It remains to be seen whether further increases in cell size and/or reductions in cooling rate will, in fact, alter this outcome.

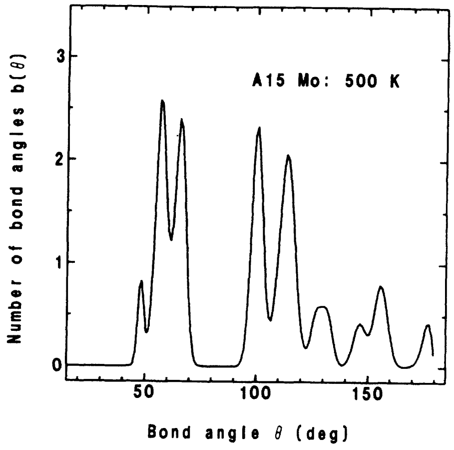

FIG. 5. Angular-correlation function $b(\theta)$ for Mo in the *A* 15 structure at 500 K and $\Omega=\Omega_0$, as obtained with the multi-ion potentials v_2, v_3, and v_4.

B. Free energies and thermodynamic melting

In our second approach to melting in Mo, we have attempted to calculate accurate solid and liquid ion-thermal free-energy data over substantial ranges of volume and temperature and then determine the corresponding thermodynamic melting curve. The ion-thermal free energy in the bcc solid can be conveniently divided into quasiharmonic and anharmonic contributions:

$$A_{\text{ion}}^{\text{sol}}(\Omega,T)=A_{\text{ion}}^{\text{qh}}(\Omega,T)+A_{\text{ion}}^{\text{ah}}(\Omega,T) \; . \tag{25}$$

The former contribution can be expressed in terms of quasiharmonic phonon frequencies for the bcc lattice, $\nu_\lambda(\mathbf{q})$, by the standard thermodynamic result

$$A^{\rm qh}_{\rm ion}(\Omega,T)=k_BT\sum_{\mathbf{q},\lambda}\ln\{2\sinh[h\nu_\lambda(\mathbf{q})/(2k_BT)]\}\ , \qquad (26)$$

where the sum is over all wave vectors $\mathbf{q}$ and phonon branches λ in the first Brillouin zone. Here, the required phonons have been calculated directly in terms of tangential and radial force-constant functions, as described in Ref. 12. To evaluate the right-hand side of Eq. (26), phonon frequencies have been sampled at 1240 $\mathbf{q}$ points in the irreducible wedge of the bcc Brillouin zone. In the multi-ion-potential case, the bcc structure is found to be mechanically stable at all volumes and $A^{\rm qh}_{\rm ion}(\Omega,T)$ has been calculated in the range $68.8\leq\Omega\leq129.3$ a.u. ($0.655\leq\Omega/\Omega_0\leq1.230$; $\Omega_0=105.1$) at increments of $\Delta\Omega=6.05$ a.u. for temperatures up to 17 500 K. In the effective-pair-potential case, on the other hand, the bcc structure is mechanically *unstable* at both large and small volumes and $A^{\rm qh}_{\rm ion}$ can be evaluated only in a limited range near Ω_0: $86.95\leq\Omega\leq117.2$ a.u. Outside of this range the soft T_1 [110] phonon modes (Fig. 1) become imaginary. This makes the calculation of bcc free energies and melting with $v_2^{\rm eff}$ problematic, so we focus first on their calculation with the multi-ion potentials.

In the multi-ion-potential case, we have calculated the corresponding anharmonic bcc free-energy component, $A^{\rm ah}_{\rm ion}(\Omega,T)$, entirely from MD thermal-energy data. This is done by noting that in general

$$A^{\rm ah}_{\rm ion}(\Omega,T)=-T\int_0^T[E^{\rm ah}_{\rm ion}(\Omega,T')/(T')^2]dT'\ , \qquad (27)$$

where $E^{\rm ah}_{\rm ion}$ is the anharmonic part of the solid ion-thermal energy $E^{\rm sol}_{\rm ion}$. Since the quasiharmonic component of $E^{\rm sol}_{\rm ion}$ is just $3k_BT$ in a classical MD simulation, it follows that $E^{\rm ah}_{\rm ion}$ may be extracted from the MD data as simply

$$E^{\rm ah}_{\rm ion}(\Omega,T)=E^{\rm sol}_{\rm ion}(\Omega,T)-3k_BT\ . \qquad (28)$$

Our results for Mo are displayed in Fig. 6(a) in the form $E^{\rm ah}_{\rm ion}/3k_BT$. From this figure one can infer that $E^{\rm ah}_{\rm ion}(\Omega,T)$ is a negative and monotonically decreasing function of both volume and temperature. Its temperature dependence may be adequately represented by a polynomial expansion of the form[36]

$$E^{\rm ah}_{\rm ion}(\Omega,T)=-A_2T^2-2A_3T^3-3A_4T^4\ , \qquad (29)$$

where A_2, A_3, and A_4 are volume-dependent coefficients with $A_2>0$. Inserting Eq. (29) back in Eq. (27) then yields

$$A^{\rm ah}_{\rm ion}(\Omega,T)=A_2T^2+A_3T^3+A_4T^4\ . \qquad (30)$$

In the present study, our ion-thermal MD data for $E^{\rm ah}_{\rm ion}$ has been generated at four equally spaced volumes 80.9 and 117.2 a.u. and five equally spaced temperatures between 500 and 6500 K. At each volume a least-squares fit of this data has been done using Eq. (29). The resulting coefficients $A_n(\Omega)$ are sufficiently smoothly varying functions of volume that all needed values can be obtained by interpolation. Thus for the volumes and temperatures of interest here, $A^{\rm ah}_{\rm ion}(\Omega,T)>0$, so that the net effect of anharmonic contributions is to raise the free energy of the bcc solid and consequently lower the calculated melting temperatures.

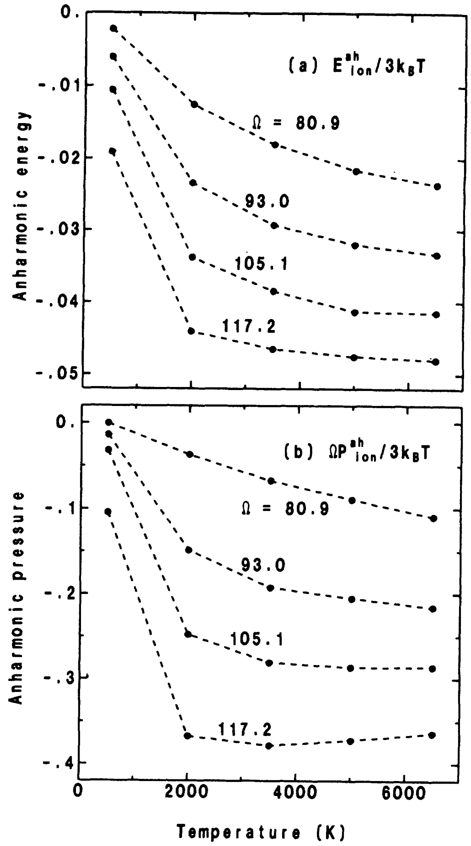

FIG. 6. Anharmonic contributions to thermal energies and pressures in bcc Mo, as given by the present multi-ion-potential MD data (solid points): (a) $E^{\rm ah}_{\rm ion}/3k_BT$; (b) $\Omega P^{\rm ah}_{\rm ion}/3k_BT$.

The corresponding anharmonic component of the ion-thermal pressure, $P^{\rm ah}_{\rm ion}$, can be obtained either by differentiating Eq. (30) with respect to volume or by directly using the MD data on the solid ion-thermal pressure, $P^{\rm sol}_{\rm ion}$, in a procedure similar to that just described. We have followed the latter course. First, $P^{\rm ah}_{\rm ion}$ is extracted from $P^{\rm sol}_{\rm ion}$ in the form

$$\Omega P^{\rm ah}_{\rm ion}(\Omega,T)=\Omega P^{\rm sol}_{\rm ion}(\Omega,T)-3k_BT\gamma(\Omega)\ , \qquad (31)$$

where γ is the high-temperature Grüneisen parameter obtained from the quasiharmonic phonons. As can be seen from Fig. 6(b), the volume and temperature dependence of $\Omega P^{\rm ah}_{\rm ion}$ is qualitatively similar to $E^{\rm ah}_{\rm ion}$. Thus its temperature dependence can be represented by an expansion analogous to Eq. (29),

$$\Omega P^{\rm ah}_{\rm ion}(\Omega,T)=-B_2T^2-2B_3T^3-3B_4T^4\ , \qquad (32)$$

where the volume-dependent coefficients $B_n(\Omega)$ are calculated in the same manner as the $A_n(\Omega)$ above.

In the liquid phase, the entire ion-thermal free energy $A^{\rm liq}_{\rm ion}$ can be obtained from the MD data, apart from an additive constant. Specifically, Eq. (27) is replaced by

$$A^{\mathrm{liq}}_{\mathrm{ion}}(\Omega,T)/T=C_0(\Omega)/T_0-\int_{T_0}^{T}[E^{\mathrm{liq}}_{\mathrm{ion}}(\Omega,T')/(T')^2]dT' \;, \quad (33)$$

where T_0 is a reference temperature and $C_0(\Omega)\equiv A^{\mathrm{liq}}_{\mathrm{ion}}(\Omega,T_0)$. Allowing for an additional term linear in T, the temperature dependence of $E^{\mathrm{liq}}_{\mathrm{ion}}$ can be represented by a generalized expansion of the form

$$E^{\mathrm{liq}}_{\mathrm{ion}}(\Omega,T)=C_1\tau-C_2\tau^2-2C_3\tau^3-3C_4\tau^4 \;, \quad (34)$$

where $\tau\equiv T/T_0$ and where C_1, C_2, C_3, and C_4 are volume-dependent coefficients with $C_1>0$ and $C_2>0$. Using this result in Eq. (33), one thus obtains

$$A^{\mathrm{liq}}_{\mathrm{ion}}(\Omega,T)=C_0\tau-C_1\tau\ln\tau+C_2\tau(\tau-1)+C_3\tau(\tau^2-1)+C_4\tau(\tau^3-1) \;. \quad (35)$$

Ion-thermal MD data for $E^{\mathrm{liq}}_{\mathrm{ion}}$ has been accumulated on the same volume mesh as for $E^{\mathrm{ah}}_{\mathrm{ion}}$ at five equally spaced temperatures between 3500 and 15 500 K. As with $E^{\mathrm{ah}}_{\mathrm{ion}}$, a least-squares fit of this data has been done at each volume, using Eq. (34). The resulting coefficients $C_n(\Omega)$ are again reasonably smooth functions of Ω which can be interpolated at all required values. Similarly, the temperature dependence of $\Omega P^{\mathrm{liq}}_{\mathrm{ion}}$ can be represented by the expansion

$$\Omega P^{\mathrm{liq}}_{\mathrm{ion}}(\Omega,T)=D_1\tau-D_2\tau^2-2D_3\tau^3-3D_4\tau^4 \;, \quad (36)$$

with the volume-dependent coefficients $D_n(\Omega)$ determined from the MD data in the same manner as the $C_n(\Omega)$.

The natural reference temperature of the liquid is $T_0=\infty$, where one reaches the ideal-gas limit and $C_0(\Omega)$ is known exactly. This limit is impractical to consider here, however, because $E^{\mathrm{liq}}_{\mathrm{ion}}$ cannot be reliably calculated above 50 000 K, as previously indicated.[35] Instead, we have developed a special trick to obtain C_0 within our calculable temperature range. We recall that above 15 500 K the ion-thermal energy $E^{\mathrm{liq}}_{\mathrm{ion}}(\Omega,T)$ for the multi-ion-potential case is essentially the same as for the effective-pair-potential case. It follows from Eq. (33) that $A^{\mathrm{liq}}_{\mathrm{ion}}(\Omega,T)$ is also the same for the two cases above that temperature, and one can thus choose $T_0=15\,500$ K and attempt to determine C_0 from v_2^{eff} alone. This allows one to introduce the powerful techniques of modern fluid theory for calculating free energies from pair potentials. Specifically, we use variational perturbation theory[37–39] (VPT) based on an r^{-12} reference system whose free energy and pair-correlation function are accurately known.[38] In VPT an upper bound on the liquid free energy A_{liq} is established by the rigorous Gibbs-Bogolyubov inequality:[37]

$$A_{\mathrm{liq}}(\Omega,T)\equiv E_0(\Omega)+A^{\mathrm{liq}}_{\mathrm{ion}}(\Omega,T)\le A^{\mathrm{max}}_{\mathrm{liq}}(\Omega,T) \;, \quad (37)$$

where

$$A^{\mathrm{max}}_{\mathrm{liq}}(\Omega,T)=E_{\mathrm{vol}}(\Omega)+A_{\mathrm{ref}}(z)+(2\pi/\Omega)\int_0^\infty g_{\mathrm{ref}}(r;z)[v_2^{\mathrm{eff}}(r;\Omega)-v_{\mathrm{ref}}(r;z)]r^2dr \;. \quad (38)$$

Here A_{ref}, g_{ref}, and v_{ref} are the free energy, pair-correlation function, and pair potential of the reference system with

$$v_{\mathrm{ref}}(r;z)=\epsilon(\sigma/r)^{12} \quad (39)$$

and $z=(\sigma^3/\sqrt{2}\Omega)(\epsilon/k_BT)^{1/4}$. At each volume and temperature of interest, the variational parameter z can be chosen to minimize the right-hand side of Eq. (38), so that in practice $A^{\mathrm{max}}_{\mathrm{liq}}$ becomes a very close upper bound to the true liquid free energy A_{liq}. A corresponding lower bound on the free energy can be established in the form[39]

$$A_{\mathrm{liq}}(\Omega,T)\ge A^{\mathrm{min}}_{\mathrm{liq}}(\Omega,T) \;, \quad (40)$$

where

$$A^{\mathrm{min}}_{\mathrm{liq}}(\Omega,T)=E_{\mathrm{vol}}(\Omega)+A_{\mathrm{ref}}(z)+(2\pi/\Omega)\int_0^\infty g(r)[v_2^{\mathrm{eff}}(r;\Omega)-v_{\mathrm{ref}}(r;z)]r^2dr \;. \quad (41)$$

Here $g(r)$ is the true pair-correlation function for v_2^{eff} and is determined from our MD simulations. The variational parameter z can now be chosen to maximize $A^{\mathrm{min}}_{\mathrm{liq}}$, making it a close lower bound to A_{liq}. A very accurate value of A_{liq} is then calculated by taking the average[39]

$$A_{\mathrm{liq}}(\Omega,T)=\tfrac{1}{2}[A^{\mathrm{min}}_{\mathrm{liq}}(\Omega,T)+A^{\mathrm{max}}_{\mathrm{liq}}(\Omega,T)] \;. \quad (42)$$

In this work, we have applied the above VPT equations at the volume $\Omega=\Omega_0$ and temperature $T=T_0=15\,500$ K, so that

$$C_0(\Omega_0)=A_{\mathrm{liq}}(\Omega_0,T_0)-E_0(\Omega_0) \;, \quad (43)$$

with $A_{\mathrm{liq}}(\Omega_0,T_0)$ determined by Eq. (42). The volume dependence of C_0 has then been obtained by noting that

$$C_0(\Omega)=C_0(\Omega_0)-\int_{\Omega_0}^{\Omega}P^{\mathrm{liq}}_{\mathrm{ion}}(\Omega,T_0)d\Omega \quad (44)$$

and using Eq. (36) for $P^{\mathrm{liq}}_{\mathrm{ion}}$. We have verified that the final ion-thermal free energy (35) is insensitive to the choice of temperature used in Eq. (42) by repeating the VPT calculation at $T=50\,000$ K and then using Eq. (33) to determine $C_0(\Omega_0)$.

Finally, the components of the solid and liquid free energies can be reassembled and the ion-thermal melting curve determined. We have for the bcc solid

$$A_{\rm sol}(\Omega,T)=E_0(\Omega)+k_BT\sum_{\mathbf{q},\lambda}\ln\{2\sinh[h\nu_\lambda(\mathbf{q})/(2k_BT)]\}+A_2T^2+A_3T^3+A_4T^4 \quad (45)$$

and for the liquid

$$A_{\rm liq}(\Omega,T)=E_0(\Omega)+C_0\tau-C_1\tau\ln\tau+C_2\tau(\tau-1)+C_3\tau(\tau^2-1)+C_4\tau(\tau^3-1)\ . \quad (46)$$

Points along the ion-thermal melting curve have been determined by making a common-tangent construction between $A_{\rm sol}(\Omega,T)$ and $A_{\rm liq}(\Omega,T)$ at temperature increments of 500 K up to 17 500 K. The resulting melting curve below 1 Mbar is shown in Fig. 7 and is compared with the single dynamic melting point obtained from our constant-volume simulation at $\Omega=\Omega_0$. It is seen that the latter point lies exactly on the free-energy-based melting curve. This indicates that, in contrast to the large amount of supercooling of the liquid observed in our MD simulations, no significant superheating of the solid has occurred in the multi-ion-potential case.

In the effective-pair-potential case, we have attempted to obtain anharmonic and liquid free energies from MD data only at $\Omega=\Omega_0$. While in the liquid this was entirely successful, in the solid the marginal stability of the bcc structure gave rise to substantial fluctuations in thermal energies and pressures, such that a meaningful anharmonic free-energy contribution could not be determined. We have, however, been able to obtain reasonable anharmonic and liquid free-energy estimates from simpler approaches. In the solid, we have used a standard cell model[40] to obtain bcc anharmonic contributions over the limited volume range where the bcc structure is stable. In the liquid, we have used VPT with $A_{\rm liq}$ approximated by $A_{\rm liq}^{\rm max}$, as given by Eq. (38). From these results, an ion-thermal melting curve has been determined between about 0.1 and 0.7 Mbar and this is plotted as the dashed line in Fig. 7. In contrast to the multi-ion-potential case, it is seen that the corresponding dynamic melting point lies about 1000 K higher in temperature than this curve, suggesting that some superheating of the solid did occur in the effective-pair-potential simulations. On the other hand, the melting curve obtained from $v_2^{\rm eff}$ is consequently in rather good agreement with the multi-ion-potential result over the limited range where the former can be calculated. Considering the more approximate nature of the effective-pair-potential free energies, however, this close agreement may be somewhat accidental.

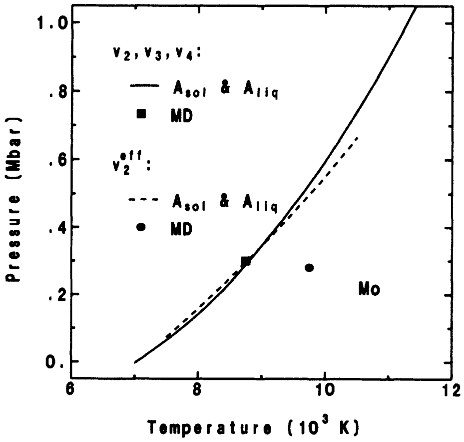

FIG. 7. Ion-thermal melting curves for Mo obtained from multi-ion-potential and effective-pair-potential free energies, as discussed in the text. Also shown are corresponding dynamical melting points obtained directly from the MD simulations at $\Omega=\Omega_0$.

IV. ELECTRON-THERMAL CONTRIBUTIONS AND THE FULL MELT CURVE

To complete the full melting calculation in the multi-ion-potential case, we must finally renomalize the above ion-thermal result by adding appropriate electron-thermal free-energy contributions to $A_{\rm sol}$ and $A_{\rm liq}$. We here calculate the electron-thermal free energy from the standard low-temperature expression valid for $k_BT \ll E_F$,

$$A_{\rm el}(\Omega,T)=-\frac{\pi^2}{6}\rho(E_F)(k_BT)^2\ , \quad (47)$$

where $\rho(E_F)$ is the density of states at the Fermi level. The corresponding electron-thermal energy and pressure are just $E_{\rm el}=-A_{\rm el}$ and $P_{\rm el}=-\partial A_{\rm el}/\partial\Omega$, respectively. These equations are straightforward to apply in the case of the solid, where the density of states can be obtained directly from self-consistent electronic-structure calculations. We have applied the LMTO method to calculate both the bcc and fcc DOS as a function of volume Ω. The results for $\Omega=\Omega_0$ are plotted in Fig. 8. The bcc DOS shows the expected deep valley in the vicinity of E_F, and $\rho(E_F)$ is found to vary slowly and smoothly with volume, as shown in Fig. 9. This is in sharp contrast to the fcc DOS which has a sharply peaked structure near E_F and consequently a much larger value of $\rho(E_F)$ which also varies more rapidly with volume.

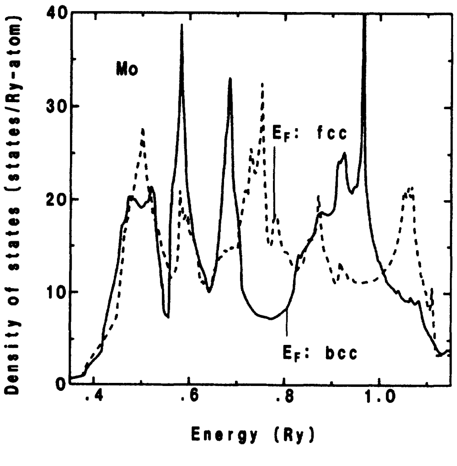

FIG. 8. Density of states for bcc and fcc Mo at $\Omega=\Omega_0$, as obtained from the present self-consistent LMTO electronic-structure calculations.

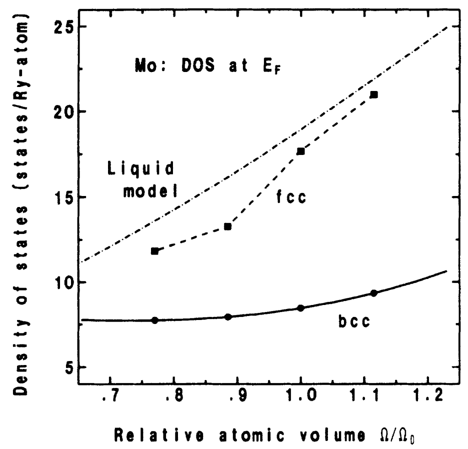

FIG. 9. Density of states at the Fermi level, $\rho(E_F)$, as a function of volume for bcc, fcc, and liquid Mo. The bcc and fcc results are from self-consistent LMTO calculations, while the liquid result is from the simplified model discussed in the text.

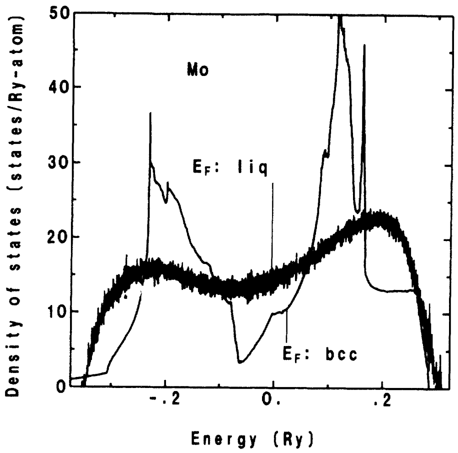

FIG. 10. Canonical-d-band density of states for bcc and liquid Mo at $\Omega=\Omega_0$ obtained from tight-binding calculations, as discussed in the text.

In the liquid, on the other hand, we have no comparable means at present of calculating a self-consistent density of states, but we have been able to formulate a simple, realistic model which can be quantitatively verified. In this model we take the liquid DOS as a sum of a free-electron sp component ρ_{sp}, and a Friedel-model[41,42] d-electron component ρ_d. At the Fermi level in Mo one has

$$\rho(E_F)=\rho_{sp}(E_F)+\rho_d(E_F)=\tfrac{2}{3}Z/E_F+10/W_d\ , \qquad (48)$$

where Z is the number of s and p electrons per atom and W_d is the d-band width. The quantities Z, E_F, and W_d are all volume dependent but structure insensitive and thus can be taken from our first-principles calculations on the bcc phase. This leads to the liquid model result for $\rho(E_F)$ plotted in Fig. 9. Note that the magnitude and volume dependence of the liquid-model $\rho(E_F)$ is similar to that for the close-packed fcc structure, which is physically quite reasonable.

To verify the quantitative adequacy of the dominant d-band term in Eq. (48), we have also done a series of canonical-d-band tight-binding calculations of both the bcc and liquid DOS in Mo. In these calculations, the liquid has been approximated as a simple cubic structure with a basis of 250 ions whose coordinants are established by our liquid MD simulations at 3500 K and $\Omega=\Omega_0$. This has been done for a total of ten (randomly chosen) MD ion configurations and the resulting DOS's averaged. The configuration-averaged liquid DOS so obtained is plotted in Fig. 10 and compared with the corresponding bcc result. The expected dramatic change in the density of states in going from bcc to the liquid is clearly evident in this figure. In particular, note the elimination of the deep valley near E_F and the rise in $\rho(E_F)$. In Fig. 11 the same liquid DOS is compared with the Friedel model used in Eq. (48). As desired, near $E=E_F$ the Friedel model does give a quantitatively accurate value of the DOS.

With $\rho(E_F)$ established for the bcc solid from our

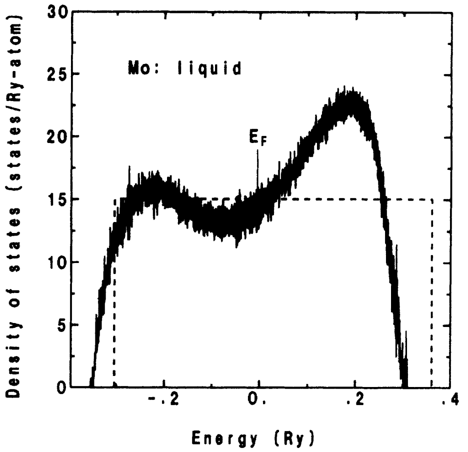

FIG. 11. Liquid density of states for Mo as in Fig. 10 compared against the simple Friedel model (dashed lines).

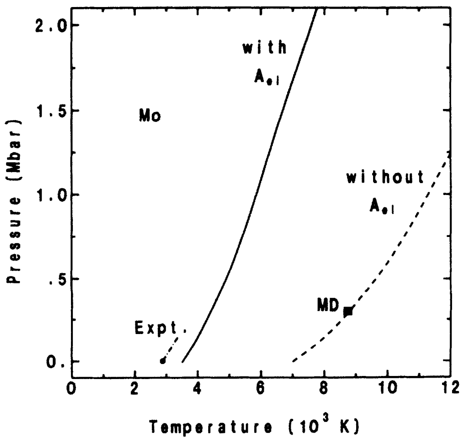

FIG. 12. Melting curves for Mo obtained from multi-ion-potential free energies with and without the electron-thermal component A_{el}. Also shown is the dynamical ion-thermal melting point obtained from MD simulations at $\Omega=\Omega_0$ and the experimental melting point and initial slope from Ref. 13.

TABLE II. Melting properties of Mo at zero pressure. Quantities and units: melting temperature T_m in K; solid and liquid volumes Ω_{sol} and Ω_{liq} in a.u.; $\Delta\Omega = \Omega_{\text{liq}} - \Omega_{\text{sol}}$; latent heat L in mRy/atom; entropy change ΔS in k_B; melting-curve slope dP_m/dT_m in kbar/K; and liquid specific heat c_p^{liq} in k_B.

Quantity	Present theory	Experiment (Ref. 13)
T_m	3528	2883
Ω_{sol}	110.1	110.3
Ω_{liq}	114.1	115.0
$\Delta\Omega$	4.0	4.6
L	27.9	27.3
$\Delta S/k_B$	1.25	1.49
dP_m/dT_m	0.29	0.30
c_p^{liq}/k_B	5.4	8.5; 7.1[a]; 4.2[b]

[a] Reference 14.

[b] Reference 15.

LMTO calculations and for the liquid from Eq. (48), we have calculated respective electron-thermal free-energy contributions $A_{\text{el}}^{\text{sol}}$ and $A_{\text{el}}^{\text{liq}}$ using Eq. (47) and then added these results to Eqs. (45) and (46) for A_{sol} and A_{liq}. A full melting curve has then been calculated in the same manner as described above for the ion-thermal result. The respective melting curves with and without A_{el} are compared in Fig. 12. The large increase in $\rho(E_F)$ for the liquid is directly reflected in a factor of 2 lowering of the calculated melting temperatures with A_{el} included. The final melting temperatures are now reduced to the desired range, but near zero pressure remain about 20% higher than experiment. As demonstrated in Table II, however, other calculated zero-pressure melting properties are in quite good agreement with experiment.[13–15] This is particularly so for the solid and liquid volumes, the latent heat, and the initial slope of the melting curve. As expected, a large value of the liquid specific heat c_p^{liq} is also obtained due to the extra contribution from A_{el}. Our calculated value of 5.4 k_B is intermediate between those of 4.2 and 8.5 k_B measured from drop-calorimetry[15] and in isobaric-expansion experiments,[13] respectively.

V. CONCLUSIONS

The present study on Mo has shed considerable light on the importance of angular forces and electron-thermal contributions to the high-temperature properties of central bcc transition metals. As we had expected from our previous zero-temperature studies,[5,12] angular forces play a central and critical role in determining structural phase stability in the solid at all temperatures, and these forces are rather well described in Mo by MGPT multi-ion potentials. The competitive nature of the metastable $A15$ structure with bcc is a natural consequence of these forces and, as our MD results demonstrate, they can control the qualitative freezing behavior of the liquid. Somewhat more surprising is the apparent minimal effect of these forces above the melting transition, where the effective-pair potential v_2^{eff} yields a reasonably good description of both the structural and thermodynamic properties of the liquid. Moreover, this description improves rapidly with increasing temperature and becomes quantitatively accurate at high temperature. This would seem to provide considerable justification for treating liquid transition metals in the future with such pair potentials. At the same time, the present effective-pair potential does not lead to a satisfactory ion-thermal melting curve, due in large part to unphysically soft T_1 [110] phonon modes it produces in the bcc solid. Refinements in the potential might improve this situation, but the present study suggests that reliable calculation of the vibrational and ion-thermal melting properties of bcc transition metals requires the angular forces.

The unusually big impact of electron-thermal contributions in lowering the melting temperature of Mo is a direct consequence of the large and strongly phase-dependent density of electronic states in such central transition metals. We expect that this effect is probably maximized in the bcc metals, especially the group-VIB metals, where the positioning of the Fermi level of the solid in the midst of a deep valley in the DOS ensures a dramatic change upon melting. However, the possible importance of electron-thermal effects on any high-temperature phase transition in transition metals clearly needs to be investigated on a case by case basis. In the context of melting, one would ideally like to have comparable methods of treating the solid and liquid DOS. While our simple model DOS seems well justified in liquid Mo, we do not expect this model to have general validity in other transition metals. In the future it may be possible to apply the self-consistent LMTO method to the liquid in the same manner as we have done the present tight-binding calculations, but this will require a basis of far fewer than the 250 ions treated here.

Finally, we believe this work has amply demonstrated the feasibility of doing comprehensive MD simulation studies on central transition metals using MGPT multi-ion potentials. The techniques developed here together with the experience gained on Mo should be directly applicable to the phase diagrams of other similar materials. One such application of great current interest is to the high-pressure, high-temperature phase stability and melting in iron, and preliminary work on this problem has been initiated.[43] Beyond bulk structural and thermodynamic properties and elemental phase diagrams, it should also be possible to extend the present MD capabilities to defects and surfaces in the context of a recently developed extension of the GPT,[44] in which the cohesive-energy functional (1) is transformed to an appropriate local-environment representation involving a modulated volume term and modulated bulk potentials. In this regard, the present refined MGPT potentials have been successfully tested on the free-surface energetics of Mo in the same manner as discussed in Ref. 44 for the scheme-1 potentials of Ref. 12.

ACKNOWLEDGMENTS

This work was performed under the auspices of the U.S. Department of Energy by Lawrence Livermore National Laboratory (LLNL) under Contract No. W-7405-Eng-48. The author wishes to thank Dr. S. M. Foiles and

Dr. A. K. McMahan for communicating their total-energy results on the *A* 15 structure prior to publication. The author would also like to acknowledge valuable assistance from Dr. J. E. Klepeis in setting up the tight-binding calculations on bcc and liquid Mo. These calculations were performed with a general-purpose electronic-structure code provided to LLNL by Dr. M. van Schilfgaarde.

APPENDIX

In this appendix we discuss the derivations of Eqs. (17) and (18) for the three- and four-ion forces $F_i^{(3)}$ and $F_i^{(4)}$, respectively, together with a few details about the implementation of these results in MD simulation. The basic property of the GPT potentials that one requires in these derivations is that $v_3(ijk)$ and $v_4(ijkl)$ are symmetric with respect to the interchange of any two indices. This symmetry property first implies that differentiation of v_3 and v_4 with respect to one ion coordinate is equivalent to differentiation with respect to another when all coordinates are summed. One can thus immediately express the forces in the form

$$\mathbf{F}_i^{(3)} = -\frac{\partial}{\partial \mathbf{R}_i}\left[\frac{1}{6}\sum_{i,j,k}{}' v_3(ijk)\right] = -\frac{1}{2}\sum_{j,k}{}' \frac{\partial v_3(ijk)}{\partial \mathbf{R}_i} \tag{A1}$$

and

$$\begin{aligned}\mathbf{F}_i^{(4)} &= -\frac{\partial}{\partial \mathbf{R}_i}\left[\frac{1}{24}\sum_{i,j,k,l}{}' v_4(ijkl)\right] \\ &= -\frac{1}{6}\sum_{j,k,l}{}' \frac{\partial v_4(ijkl)}{\partial \mathbf{R}_i} .\end{aligned} \tag{A2}$$

One then notes from Eqs. (3) and (4) how v_3 and v_4 depend on interatomic separations R_{ij}, etc., and uses the chain rule, as in Eq. (16), to express the derivative with respect to $\mathbf{R}_i$ in terms of derivatives with respect to the separations R_{ij}, R_{ki}, and R_{li}. This yields

$$\mathbf{F}_i^{(3)} = -\frac{1}{2}\sum_{j,k}{}' \left[\frac{\partial v_3(ijk)}{\partial R_{ij}}\hat{\mathbf{R}}_{ij} - \frac{\partial v_3(ijk)}{\partial R_{ki}}\hat{\mathbf{R}}_{ki}\right] \tag{A3}$$

and

$$\begin{aligned}\mathbf{F}_i^{(4)} = -\frac{1}{6}\sum_{j,k,l}{}' \Bigg[&\frac{\partial v_4(ijkl)}{\partial R_{ij}}\hat{\mathbf{R}}_{ij} - \frac{\partial v_4(ijkl)}{\partial R_{li}}\hat{\mathbf{R}}_{li} \\ &- \frac{\partial v_4(ijkl)}{\partial R_{ki}}\hat{\mathbf{R}}_{ki}\Bigg] .\end{aligned} \tag{A4}$$

To arrive at the final result for $\mathbf{F}_i^{(3)}$, one used the facts that $R_{ik} = R_{ki}$ and $\hat{\mathbf{R}}_{ik} = -\hat{\mathbf{R}}_{ki}$ and then interchanges the coordinates j and k in the second term in Eq. (A3). The second term is thus equal to the first, since $v_3(ikj) = v_3(ijk)$ and Eq. (17) follows. For $\mathbf{F}_i^{(4)}$, one can show in the same manner that the second and third terms in Eq. (A4) are equal to the first, so that Eq. (18) also follows immediately.

One can generalize the above results to any $n \geq 2$ in the form

$$\mathbf{F}_i^{(n)} = -\frac{1}{(n-2)!}\sum_{j,k,\ldots}{}' \frac{\partial v_n(ijk\ldots)}{\partial R_{ij}}\hat{\mathbf{R}}_{ij} . \tag{A5}$$

In practice, it is also convenient to re-express the forces as

$$\mathbf{F}_i^{(n)} = \sum_j{}' \mathbf{F}_{ij}^{(n)} \tag{A6}$$

and exploit the additional symmetry property that $\mathbf{F}_{ji}^{(n)} = -\mathbf{F}_{ij}^{(n)}$. This results in a factor of 2 computational-time savings when accumulating the forces during a given time step in an MD simulation. For $n = 2$, 3, and 4, the $\mathbf{F}_{ij}^{(n)}$ are given by

$$\mathbf{F}_{ij}^{(2)} = -\frac{\partial v_2(ij)}{\partial R_{ij}}\hat{\mathbf{R}}_{ij} , \tag{A7}$$

$$\mathbf{F}_{ij}^{(3)} = -\sum_k{}' \frac{\partial v_3(ijk)}{\partial R_{ij}}\hat{\mathbf{R}}_{ij} , \tag{A8}$$

and

$$\mathbf{F}_{ij}^{(4)} = -\frac{1}{2}\sum_{k,l}{}' \frac{\partial v_4(ijkl)}{\partial R_{ij}}\hat{\mathbf{R}}_{ij} = -\sum_{k<l} \frac{\partial v_4(ijkl)}{\partial R_{ij}}\hat{\mathbf{R}}_{ij} . \tag{A9}$$

Since $\mathbf{F}_{ij}^{(4)}$ is by far the most time consuming of the three components to evaluate, the second form of Eq. (A9) results in an additional factor of 2 time savings when calculating the forces.

One can further note that the virial components of the pressure, $P_{\rm vir}^{(n)}$, are readily expressed in terms of the $\mathbf{F}_{ij}^{(n)}$:

$$P_{\rm vir}^{(n)} = \frac{1}{6\Omega N}\sum_{i,j}{}' \mathbf{R}_{ij}\cdot\mathbf{F}_{ij}^{(n)} = \frac{1}{3\Omega N_i}\sum_{i<j} \mathbf{R}_{ij}\cdot\mathbf{F}_{ij}^{(n)} . \tag{A10}$$

These components must be combined with the direct volume components

$$P_{\rm vol} = -dE_{\rm vol}/d\Omega \tag{A11}$$

and

$$P_{\rm vol}^{(n)} = -\frac{1}{n!N}\sum_{i,j,k\ldots}{}' \frac{\partial v_n(ijk\ldots)}{\partial \Omega} \tag{A12}$$

to calculate the total pressure. In an MD simulation, it is most efficient to calculate the energy, pressure, and forces at the same point during a time step. This necessitates calculating the potentials v_n and their derivatives $\partial v_n/\partial R_{ij}$ and $\partial v_n/\partial \Omega$ for a given ion configuration. The pair-potential terms v_2, $\partial v_2/\partial R_{ij}$, and $\partial v_2/\partial \Omega$ present no difficulty in this regard and can be evaluated by direct interpolation from corresponding one-dimensional tables. For the multi-ion-potential terms, however, the analytic nature of v_3 and v_4 in the MGPT now becomes of crucial importance. As can be inferred from Eqs. (9) and (10), the explicit volume dependence of these potentials is contained in a prefactor of each term. Thus the volume derivative of each term is proportional to the term itself, so that $\partial v_3/\partial \Omega$ and $\partial v_4/\partial \Omega$ can be evaluated directly from the corresponding components of v_3 and v_4. The analytic forms of $\partial v_3/\partial R_{ij}$ and $\partial v_4/\partial R_{ij}$, on the other hand, are much more complicated due to the complex nature of the angular functions L, P, and M. It is more efficient in this case to calculate these derivatives numerically. Because the multi-ion potentials themselves are analytic, this can be done very accurately by evaluating v_3 and v_4 at a second ion configuration only infinitesimally displaced from the first. Thus all multi-ion terms can be evaluated by calculating v_3 and v_4 exactly twice at each time step.

The inclusion of three- and four-ion angular forces in the MGPT necessarily means that our multi-ion MD simulations are much more time consuming than ones which include radial forces alone, such as those with $v_2^{\rm eff}$. Nevertheless, the above scheme is quite tractable, especially if implemented on a state-of-the-art workstation or via parallel processing. Depending on the computing environment and the specific application, one can expect running times in the range of 0.02 to 0.2 seconds per time step per ion with this scheme. In this regard, all of the multi-ion MD calculations presented in this paper have been performed on an IBM RISC/6000 model-320 workstation, which is at least a factor of 2 *slower* than state-of-the-art models, with an average running time of about 0.18 seconds per time step per ion. We also believe that multi-ion MD simulations can probably be made considerably faster in the future by finding an optimized representation of the four-ion angular function M, the evaluation of which is the single most time-consuming operation during each time step.

---

[1] R. S. Hixson, D. A. Boness, J. W. Shaner, and J. A. Moriarty, Phys. Rev. Lett. **62**, 637 (1989).

[2] Y. K. Vohra and A. L. Ruoff, Phys. Rev. B **42**, 8651 (1990).

[3] A. L. Ruoff, H. Xia, H. Luo, and Y. K. Vohra, Rev. Sci. Instrum. **61**, 3830 (1990); A. L. Ruoff, H. Xia, and Q. Xia, *ibid.* **63**, 4342 (1992).

[4] H. J. Song, K. Ghandehari, and Y. K. Vohra, Scr. Metall. **26**, 1395 (1992); G. Gu and Y. K. Vohra, Phys. Rev. B **47**, 11 559 (1993).

[5] J. A. Moriarty, Phys. Rev. B **45**, 2004 (1992).

[6] W. R. Morcom, W. L. Worrell, H. G. Sell, and H. I. Kaplan, Metall. Trans. **5**, 155 (1974).

[7] L. Cortella, B. Vinet, P. J. Desre, A. Pasturel, A. T. Paxton, and M. van Schilfgaarde, Phys. Rev. Lett. **70**, 1469 (1993).

[8] S. M. Foiles, Phys. Rev. B **48**, 4287 (1993); S. M. Foiles and A. F. Wright (unpublished).

[9] A. K. McMahan (private communication); A. K. McMahan, J. E. Klepeis, M. van Schilfgaarde, and M. Methfessel (unpublished).

[10] J. A. Moriarty, Phys. Rev. B **38**, 3199 (1988).

[11] W. Kohn and L. J. Sham, Phys. Rev. **140**, A1133 (1965); L. Hedin and B. I. Lundqvist, J. Phys. C **4**, 2064 (1971).

[12] J. A. Moriarty, Phys. Rev. B **42**, 1609 (1990).

[13] J. W. Shaner, G. R. Gathers, and C. Minichino, High Temp. High Pressures **9**, 331 (1977).

[14] I. Ya. Dikhter and S. V. Lebedev, Teplofiz. Vys. Temp. **9**, 929 (1971) [High Temp. (USSR) **9**, 845 (1971)].

[15] J. F. Treverton and J. L. Margrave, in *Proceedings of the Fifth Symposium on Thermophysical Properties,* edited by C. F. Bonilla (American Society of Mechanical Engineers, New York, 1970), p. 489.

[16] J. W. Shaner, G. R. Gathers, and W. M. Hodson, in *Proceedings of the Seventh Symposium on Thermophysical Properties,* edited by A. Cezairliyan (American Society of Mechanical Engineers, New York, 1977), p. 896.

[17] G. R. Gathers, J. W. Shaner, R. S. Hixson, and D. A. Young, High Temp. High Pressures **11**, 653 (1979).

[18] R. S. Hixson and M. A. Winkler, Int. J. Thermophys. **11**, 709 (1990).

[19] O. K. Andersen, Phys. Rev. B **12**, 3060 (1975); O. K. Andersen and O. Jepsen, Physica **91B**, 317 (1977).

[20] H. L. Skriver, *The LMTO Method* (Springer, Berlin, 1984).

[21] C. Kittel, *Introduction to Solid State Physics,* 5th ed. (Wiley, New York, 1976), p. 74.

[22] D. L. Davidson and F. R. Brotzen, J. Appl. Phys. **39**, 5768 (1968).

[23] K. W. Katahara, M. H. Manghnani, and E. S. Fisher, J. Phys. F **9**, 773 (1979).

[24] K. Maier, M. Peo, B. Saile, H. E. Schaefer, and A. Seeger, Philos. Mag. A **40**, 701 (1979).

[25] I. A. Schwirtlich and H. Schultz, Philos. Mag. A **41**, 91 (1980).

[26] R. Ziegler and H. E. Schaefer, in *Vacancies and Interstitials in Metals and Alloys,* edited by C. Abromeit and H. Wollenberger (Trans Tech, Aedermannsdorf, Switzerland, 1987), p. 145.

[27] B. M. Powell, P. Martel, and A. D. B. Woods, Can. J. Phys. **55**, 1601 (1977).

[28] M. Alouani, R. C. Albers, and M. Methfessel, Phys. Rev. B **43**, 6500 (1991).

[29] K.-M. Ho, C.-L. Fu, and B. N. Harmon, Phys. Rev. B **29**, 1575 (1984).

[30] Y. Chen, C.-L. Fu, K.-M. Ho, and B. N. Harmon, Phys. Rev. B **31**, 6775 (1985).

[31] G. H. Campbell, S. M. Foiles, P. Gumbsch, M. Rühle, and W. E. King, Phys. Rev. Lett. **70**, 449 (1993).

[32] W. G. Hoover, A. J. C. Ladd, and B. Moran, Phys. Rev. Lett. **48**, 1818 (1982); D. J. Evans, J. Chem. Phys. **78**, 3297 (1983).

[33] M. P. Allen and D. J. Tildesley, *Computer Simulation of Liquids* (Oxford University Press, Oxford, 1989).

[34] W. G. Hoover, *Computational Statistical Mechanics* (Elsevier, Amsterdam, 1991).

[35] Above 50 000 K, certain numerical problems begin to appear in our MD simulations, associated with the deep interpenetration of the large ion cores, and we have not attempted to go higher in temperature.

[36] R. E. Swanson, G. K. Straub, B. L. Holian, and D. C. Wallace, Phys. Rev. B **25**, 7807 (1982).

[37] N. W. Ashcroft and D. Stroud, in *Solid State Physics,* edited by F. Seitz, D. Turnbull, and H. Ehrenreich (Academic, New York, 1978), Vol. 33, p. 1 and references therein.

[38] D. A. Young and F. J. Rogers, J. Chem. Phys. **81**, 2789 (1984).

[39] D. B. Boercker and D. A. Young, Phys. Rev. A **40**, 6379 (1989).

[40] D. A. Young and M. Ross, J. Chem. Phys. **74**, 6950 (1981).

[41] J. Friedel, in *The Physics of Metals,* edited by J. M. Ziman (Cambridge, New York, 1969), p. 340.

[42] W. A. Harrison, *Electronic Structure and the Properties of Solids* (Freeman, San Francisco, 1980), p. 494.

[43] J. A. Moriarty, in *Proceedings of the 1993 Joint AIRAPT/APS Topical Conference on High Pressure and Technology,* edited by S. Schmidt (American Institute of Physics, New York, in press).

[44] J. A. Moriarty and R. Phillips, Phys. Rev. Lett. **66**, 3036 (1991).